Development of PZT and PZN-PT Based Unimorph Actuators for Micromechanical Flapping Mechanisms

Metin Sitti, Domenico Campolo*, Joseph Yan, Ronald S. Fearing
Dept. of EECS, University of California, Berkeley, CA 94720
*Scuola Superiore Sant'Anna, MiTech Laboratory, Pisa, Italy
Tao Su, David Taylor, Timothy D. Sands
Dept. of Materials Science and Engineering, University of California, Berkeley, CA 94720
{sitti,ronf}@eecs.berkeley.edu

Abstract

This paper focuses on the design, fabrication and characterization of unimorph actuators for a microaerial flapping mechanism. PZT-5H and PZN-PT are investigated as piezoelectric layers in the unimorph actuators. Design issues for microaerial flapping actuators are discussed, and criteria for the optimal dimensions of actuators are determined. For low power consumption actuation, a square wave based electronic driving circuit is proposed. Fabricated piezoelectric unimorphs are characterized by an optical measurement system in quasi-static and dynamic mode. Experimental performance of PZT-5H and PZN-PT based unimorphs is compared with desired design specifications. A 1 d.o.f. flapping mechanism with a PZT-5H unimorph is constructed, and 180° stroke motion at 95 Hz is achieved. Thus, it is shown that unimorphs could be promising flapping mechanism actuators.

1 Introduction

Actuators are one of the most significant integral parts of robotic mechanisms. Flapping mechanisms [1], [2], [3] require actuators with large periodic stroke (rotational) motion $(30 - 150^o)$ at high speed (10-100s of Hz) with large output forces for overcoming the aerodynamic damping. Moreover, light weight (10s of mg), high efficiency, long life time, and compact size are important issues. Piezoelectric actuators with proper design almost satisfy all of these requirements. There are different types of piezoelectric actuators such as stack [4] and bending [5] types, motors, impact type, etc. The stack type enables very high output forces although it has large size and weight, and smaller displacement relative to the bending type. Thus, flexural bending actuators generally generate large deflection with low weight. Therefore, bimorphs and unimorphs are more suitable for microaerial flapping applications [6], [3], [7]. These actuators consist of piezoelectric layers bonded to a purely elastic layer. Since they are easier to fabricate, the unimorph type is selected in this study.

Unimorph actuators have been studied by many groups [8], [9], [10], [11], [12], [13]. Its one dimensional beam theory is well established [8]. Characteristic parameters based on this theory were formulated [13]. Utilizing unimorphs in flapping mechanisms, Cox et al. [7] developed four-bar and five-bar flexure mechanisms integrated with unimorph actuators for stroke motions upto $30 - 50^o$.

Taking the microaerial flapping mechanisms as the target application in this paper, design issues, selection of the proper actuator, and its fabrication and characterization are investigated. PZT-5H and a recently developed PZN-PT single crystal material [14] are investigated as the piezoelectric layers. PZT-5H is a widely used soft piezoelectric ceramic. Strain levels as high as 1.7% can be achieved in PZN-PT depending on composition, orientation and the applied electric field. Miniature actuators are fabricated and characterized to evaluate their performance for flapping actuation.

2 Unimorph Actuators

A standard rectangular shape unimorph actuator under activation is illustrated in Figure 1. The actuator consists of a single piezoelectric layer bonded to a purely elastic layer. Steel or titanium is usually chosen for the elastic layer. When a voltage is applied across the thickness of the piezoelectric layer, longitudinal and transverse strain develop. The elastic layer opposes the transverse strain which leads to a bending deformation.
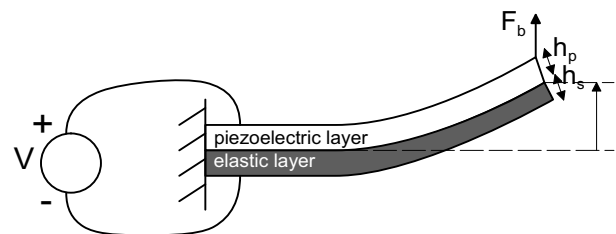

Figure 1: Basic cantilevered rectangular shape unimorph actuator structure.

2.1 Unloaded Unimorph Equations

For a free deflecting unimorph actuator, DC (low frequency) tip displacement δ_{dc}, blocking force F_b, resonant

frequency f_r, mechanical stiffness K_m, and mechanical quality factor Q_a can be written as [12], [13]:

$$\delta_{dc} = \frac{3l^2}{h_p^2}\frac{AB(B+1)}{D}d_{31}V$$

$$F_b = \frac{3wh_p}{4s_pl}\frac{AB(B+1)}{AB+1}d_{31}V$$

$$f_r = \frac{\lambda_i^2 h_p}{4\pi l^2}\sqrt{\frac{E_p}{3\rho_p}}\left[\frac{D}{(BC+1)(AB+1)}\right]$$

$$Q_a = \frac{f_r}{f_{r1}-f_{r2}}$$

$$K_m = \frac{F_b}{\delta_{dc}} = \frac{wh_p^3}{4s_pl^3}\frac{D}{AB+1} \qquad (1)$$

where $A = s_p/s_s = E_s/E_p$, $B = h_s/h_p$, $C = \rho_s/\rho_p$, $D = A^2B^4 + 2A(2B+3B^2+2B^3)+1$. Here, l is the unimorph length, w is the width, V is the applied voltage, f_{r1} and f_{r2} are the frequencies where the deflection magnitude drops to 0.707 of its resonance peak value, and d_{31} is the transverse piezoelectric coefficient. s_p and s_s are the elastic compliances, h_p and h_s are the thicknesses, E_p and E_s are the Young Moduli, and ρ_p and ρ_s are the densities of the piezoelectric and steel layers respectively, and λ_i is the eigenvalue [11] where i denotes the resonance mode, i.e. first mode $\lambda_1 = 1.875$, and the second mode $\lambda_2 = 4.694$. For the PZT-5H, PZN-PT and steel layers, Young Modulus E, density ρ, d_{31}, coupling factor k_{31}, relative dielectric constant $K_3^T = \epsilon/\epsilon_0$, and maximum electric field E_3 values are taken as in Table 1.

	PZT-5H	PZN-PT	steel
E (GPa)	61	15	193
ρ (kg/m^3)	7500	8000	7872
d_{31} (C/N)	320×10^{-12}	950×10^{-12}	$\times$
k_{31}	0.44	0.5	$\times$
K_3^T	3800	5000	$\times$
E_3 (V/m)	1.5×10^6	10×10^6	$\times$

Table 1. PZT-5H, PZN-PT and steel layer properties [1],[5].

For the design considerations, above equtions are converted to the rotational motion of the actuator for simplicity. Assuming the actuator tip deflection is small, actuator rotation angle θ_{dc}, output torque τ_a, and rotational stiffness K_a are given as follows:

$$\theta_{dc} = \frac{\delta_{dc}}{l} = \frac{3l}{h_p^2}\frac{AB(B+1)}{D}d_{31}V$$

$$\tau_a = F_bl = \frac{3wh_p}{4s_p}\frac{AB(B+1)}{AB+1}d_{31}V$$

$$K_a = K_ml^2 = \frac{wh_p^3}{4s_pl}\frac{D}{AB+1} . \qquad (2)$$

Here, the maximum input voltages are $V_{max} = E_3h_p$, e.g. for $h_p = 100$ μm, $V_{max} = 150$ V and $V_{max} = 1000$ V for PZT-5H and PZN-PT unimorphs respectively. Moreover,

the actuators are driven unipolarly, i.e. $V > 0$. Thus, the wing motion is $\phi \in [0, \phi_{dc}]$ at DC, and $\phi \in [\phi_{dc}/2 - \phi_r, \phi_{dc}/2 + \phi_r]$ at resonance.

2.2 Unimorph Fabrication Process

Commercial piezoelectric ceramics and single crystal plates were used: (1) Doped $Pb(Zr,Ti)O_3$ (PZT-5H, T105-H4E-602 ceramic single sheet, Piezo Systems, Inc.) with 127 μm thickness, and (2) $Pb(Zn_{1/3}Nb_{2/3})O_3 - PbTiO_3$ (PZN-PT, TRS Ceramics Inc.) with 136 μm thickness.

Rectangular piezoelectric and steel layers are cut using a high-speed cut-off saw (Accutom 50) with desired dimensions. For the piezo layers, the as-received thicknesses are used, and polishing is not necessary. Then, the cut layers are bonded using a thin epoxy glue (M-Bond 610, Measurement Groups Inc.) with a slight offset along the width, and cured for 24 hours at room temperature. A conductive epoxy (CW2400, Chemtronics) is applied to the side offset edge for connecting the piezo lower electrode with the steel layer. Next, wires are soldered to the steel and piezoelectric electrodes using a soldering flux (MSF-003-NI, Piezo Systems, Inc.), and the actuator is fixed to a holder for tests. Example prototypes of the PZT-5H and PZN-PT unimorphs are displayed in Figure 2. A close side view of the PZT-5H actuator is also displayed in Figure 3 for showing the piezo, steel and glue layers.
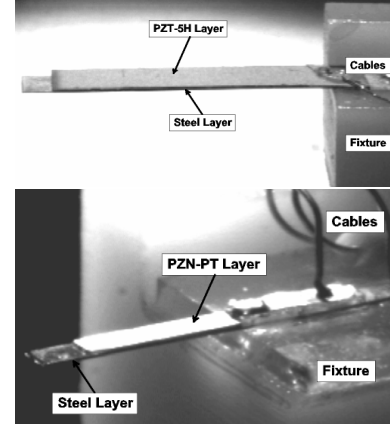

Figure 2: Photos of the prototype $16 \times 3 \times 0.21$ mm^3 PZT-5H (upper) and $5 \times 1 \times 0.22$ mm^3 size PZN-PT (lower) unimorphs.
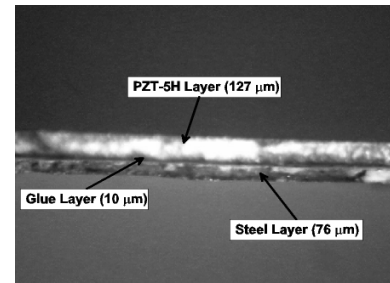

Figure 3: Side view image of the tip of the PZT-5H unimorph for showing the details of the piezo, steel and glue layers using the optical microscope.

3 Actuator Design Issues

For a flapping mechanism with a wing load on it, design parameters such as unimorph dimensions, output torque, resonant frequency, required transmission ratio, quality factor, weight, etc. are to be selected for optimal performance.
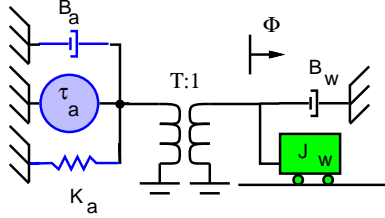

Figure 4: Linear dynamic model of piezo actuator, lossless transmission, and wing.

In our proposed flapping mechanism, a four-bar mechanism is coupled with the unimorph actuator for the stroke amplification [6], [3]. Assuming there is a wing as a load with inertia J_w and damping B_w, and a four-bar based transmission mechanism with stiffness K_t and stroke amplification (transmission ratio) T, a linear approximate dynamic modeling of Figure 4 gives:

$$J_w \ddot{\phi} + B_w \dot{\phi} + \left(\frac{K_a}{T^2} + K_t \right) \phi = \frac{\tau_a}{T} \qquad (3)$$

where ϕ is the flapping stroke angle, and K_a is the actuator rotational stiffness. Here, the actuator damping B_a and inertia J_a are assumed to be negligible with respect to the load damping and inertia.

3.1 Selection of Actuator Dimensions

For a given load power requirement, the actuator dimensions are to be chosen for ease of mechanical drive, fabrication, and drive voltage requirements. Considering a micromechanical insect modelled after a blowfly, with mass $m = 0.1$ g, wing beat of $\omega = 2\pi 150$ rad/s, and wing stroke amplitude $\phi_r = 70°$ at resonance, the net wing lift force must match the insect weight of $10^{-3}N$. Although in the quasi-steady state lift and drag forces are generally proportional to the square of velocity, we choose a linear damper with a force at peak wing velocity equals to the weight of the micromechanical flying insect (MFI) as an upper bound. (Note that the linear damper overestimates the damping force for all wing velocities less than the peak velocity). Hence the wing damping B_w (at the wing hinge) can be estimated from:

$$B_w = \frac{mgl_w}{\omega \phi_r} \qquad (4)$$

where $m = 0.1$ g, $g = 9.81$ m/s^2, l_w is the length of the wing center of pressure, and ω is the wing beat frequency. For $l_w = 10$ mm, $B_w = 8.65 \times 10^{-9} Nsm$.

The Q of a resonant system is defined as the ratio of stored energy to energy dissipated per radian. With proper actuator and transmission design, energy dissipation for the MFI is work done on moving air, i.e. useful work. A high Q hence implies large internal stored

energy, and poor controllability of wing amplitude and phase due to actuator saturation. As shown in the data by Sotavalta [15], blowflies have a relatively low Q, estimated on the order of 1-3. For the MFI, we choose the quality factor of the wing and thorax as $Q_w = 2.5$, as a higher Q_w system requires a lower transmission ratio and less actuator motion at DC.

To have a low Q_w, i.e. maneuverable wing, the wing inertia is:

$$J_w = \frac{Q_w B_w}{\omega} = 2.26 \times 10^{-11} kg \cdot m^2. \qquad (5)$$

The actuator stiffness, as seen at the wing hinge, must resonate at ω, hence:

$$K_1 = K_a/T^2 + K_t = J_w \omega^2 = 2.0 \times 10^{-5} N \cdot m \qquad (6)$$

The four-bar transmission converts the small rotation of the actuator θ to the wing rotation ϕ by a transmission ratio T. At DC, the displacement of the wing is just

$$\phi_{dc} = \frac{T\tau_a}{K_1} = \frac{2\phi_r}{Q_w} = T\theta_{dc} \qquad (7)$$

Then, for a given T and the desired wing flapping amplitude ϕ_r at resonance frequency ω:

$$\begin{aligned} \tau_a &= \frac{2K_1\phi_r}{TQ_w} = \frac{\phi_{dc}K_1}{T} \\ \theta_{dc} &= \frac{\phi_{dc}}{T} = \frac{2\phi_r}{TQ_w} \end{aligned} \qquad (8)$$

For a given h_s, h_p and V, l and w can be computed as

$$\begin{aligned} l &= \frac{h_p^2 D}{3d_{31}AB(B+1)V}\theta_{dc} \\ w &= \frac{4s_p}{3d_{31}h_pV}\frac{AB+1}{AB(B+1)}\tau_a \end{aligned} \qquad (9)$$

The average power at the wing is also another important parameter for the design which can be computed from

$$P_w = \frac{\tau_a^2 B_w}{8T^2(B_w + B_a/T^2)^2} = \frac{(mgl_w)^2 B_w}{2(B_w + B_a/T^2)^2} \qquad (10)$$

where $B_a = K_a/(Q_a\omega)$, $Q_a = 20$ and $K_a = T^2(K_1 - K_t)$.

Furthermore, the mass of the actuator m_a is limited for enabling a total flying robot mass of $m = 0.1$ g. Therefore, $m_a = (\rho_p h_p + \rho_s h_s)lw$ should be also checked.

On the other hand, the thickness ratio of PZT and elastic layers is important to select for maximum displacement and force. For a given $h_p = 127$ μm, the effect of changing h_s on the normalized values of δ_{dc}, F_b and f_r are shown in Figure 5. In the figure, depending on the design criteria, h_s could be selected to maximize δ_{dc} ($h_s = 35$ μm case), or maximize F_b (h_s is as large as possible case). In our case, since both δ_{dc} and F_b are to be maximized, the following relation is used [13] for choosing h_s:

$$h_s = \sqrt{\frac{s_s}{s_p}}h_p \qquad (11)$$

In the figure, this corresponds to $h_s = 76$ μm (dashed line). Morever, following constraints exist for h_s selection:
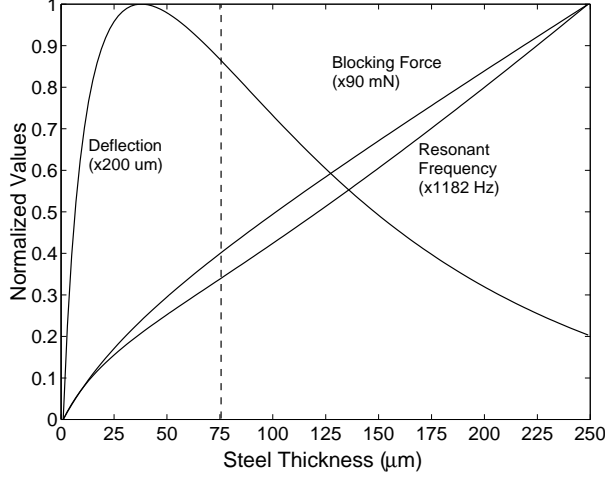
Figure 5: The effect of elastic layer thickness h_s on normalized values of the deflection δ_{dc}, the blocking force F_b, and the resonant frequency f_r for a PZT-5H unimorph with $h_p = 127\ \mu m$ and steel elastic layer.

- The resonant frequency of the actuator f_r should be around ten times larger than the desired wing beat frequency of 150 Hz in order to have a nonsignificant actuator damping at resonance, and enabling square wave driving for minimum power loss.

- Applied voltage is increased for a thicker actuator.

- During fabrication, polishing ceramic is troublesome. Therefore very thin layers are not desirable.

Using the above specifications, the MFI piezo parameters are computed as given in Table 2. Here, $J_w = 2.26 \times 10^{-11}\ kgm^2$, $B_w = 8.65 \times 10^{-9}\ Nsm$, $\omega = 2\pi150\ rad/s$, $\phi_r = 70°$, $Q_w = 2.5$, and $K_t = 5.3 \times 10^{-6}\ Nm/rad$ are taken. Considering the available piezoelectric plates we have, $V = 150\ V$ and $h_p = 127\ \mu m$, and $V = 250\ V$ and $h_p = 136\ \mu m$ are fixed for the PZT-5H and PZNT-PT layers respectively. For these values, $P_w = 4.7\ mW$. Then, for given T and h_s, l, w, F_b, δ_{dc}, P_w, f_r and m_a values are computed. From the values, it can be seen that $16 \times 3 \times 0.21\ mm^2$ size PZT-5H and $5 \times 1.3 \times 0.22\ mm^2$ size PZN-PT would enable the desired $140°$ wing flapping at 150 Hz with relatively low masses. For PZT-5H unimorph to fly, V should be increased to 250 V, lowering actuator mass to 26 mg per wing.

type	T	h_s (μm)	$l \times w$ (mm^2)	F_b (mN)	δ_{dc} (μm)	f_r (Hz)	m_a (mg)
PZT	44	76	16×2.9	54	354	464	74
PZN-PT	36	76	5×1.4	142	135	3032	12
PZT	39	50	16×3.6	49	393	406	78
PZN-PT	28	50	5×1.3	109	176	2548	10

Table 2. Selected MFI unimorph actuator parameters for different T and h_s values and unimorph types.

4 Actuator Driving Issues

4.1 Electromechanical Model

Figure 6 represents the simplified electrical equivalent of the whole system, ranging from power supply and switching stage to the wing load which is simply modeled as a linear system with inertia (L_{wing}) and damping (R_{damp}) (although this is a crude approximation it will not affect what will follow). In the figure, C_{stiff} represents the piezoelectric mechanical stiffness. For a PZT unimorph with parameters as in Table 1, $N = T$, $R_{loss} = 12\ M\Omega$, $C_l = 12\ nF$, $T_{pzt} = 6.75 \times 10^{-4}$, $C_{stiff} = 1/K_m = 0.0065\ F$, $R_{damp} = 6(T_{pzt}/T)^2\ M\Omega$, and $L_{wing} = 1/(T^2\omega^2C_{stiff}^2)$ for a given T.
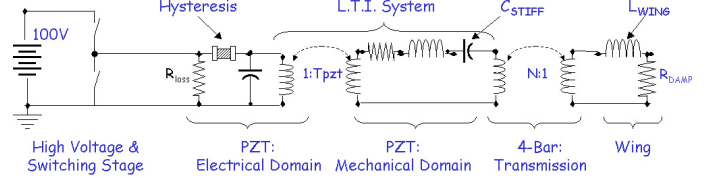

Figure 6: Electrical equivalent of the whole system where the hysteretic capacitor is the only nonlinear element.

Piezoelectric internal inertia and damping turn out to be negligible compared to the wing parameters. For the piezoelectric actuator, a model is introduced which is valid for frequencies up to resonance. More complex models which take the linear dynamics at high frequencies into account are also available. In [10], tip deflection δ, volume displacement and electrode charge q of the piezoelectric actuator are dynamically related to the moment and force F_b at the tip, uniform body pressure, and electrode voltage V by means of a 4×4 frequency-varying symmetric matrix. Since electrode voltage and current (or charge) and tip force and displacement are important in our case, only the 2×2 submatrix can be utilized:

$$\left[\begin{array}{c} \delta \\ q \end{array} \right] = \left[\begin{array}{cc} E & F \\ F & G \end{array} \right] \left[\begin{array}{c} F_b \\ V \end{array} \right] \qquad (12)$$

The Above matrix describes a 2-port electromechanical system whose electrical variables are voltage and charge while the mechanical parameters are force and displacement. An equivalent 2-port electrical system can be obtained by letting the force be represented by a voltage and displacement by a charge (i.e. mechanical speed is equivalent to current). The electrical equivalent to the 2×2 electromechanical matrix is shown in Figure 7.
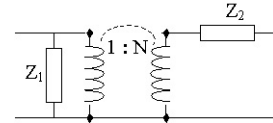

Figure 7: Electrical 2-port circuit equivalent to the electromechanical system($N = T$).

The circuit in Figure 7 completely describes the linear behavior of the piezo actuator at all frequencies, and since it is described by a linear partial differential equation (acoustic waves in piezoelectric material), Z_1, Z_2 cannot be expected to be equivalent to simple devices such as capacitors, resistors and inductors (or networks with a finite number of them) because otherwise the system in Eq. (12) could be simply described by an ordinary

differential equation. Since we are operating at low frequencies (even 10 times lower than the first mode of the actuator) the following aproximations can be used:

- $N = T$ is constant (this is valid even at frequencies higher than the first mode),

- Z_1 is a linear capacitor (the parasitic capacitance of piezoelectric materials),

- Z_2 is a RLC series impedance where R (resistor) represents damping, L (inductor) represents equivalent mass of the actuator, and C (capacitor) is related to the mechanical stiffness.

In Figure 6, the elements related to the PZT actuator are almost the same as the circuit in Figure 7. The difference is that, at the electrical port of the piezoelectric actuator two elements have been added: a resistor R_{loss} to deal with DC leakage at high fields and a nonlinear capacitor responsible for the hysteretic behavior. In [4] it has been pointed out experimentally why such hysteresis is rate independent (described by a capacitor whose voltage-charge relation is a nonlinear hysteretic function independent of frequency), and how to practically model it.

4.2 Square Wave Driving

In Figure 6, on the left, the power supply and switching stage are shown. Since power is a first concern in flying mechanisms, switching has to be used (linear drive would lead to high power consumption) together with techniques to reduce dissipation in switching capacitors [16], i.e. in this case, the parasitic capacitance of the piezoelectric actuator is the main issue. Assuming that perfect square waves are obtained from the switching stage, these waves are directly applied to the capacitor (both the linear and the hysteretic one). By connecting discharged capacitors to a power supply, high currents are produced which charge capacitors rapidly and independently from the rest of the circuit (which is mainly inductive, i.e slow to follow sudden voltage variations, and behaves as if disconnected). Also, since capacitors charge up (or even discharge in the second half of the square wave) much faster than any other voltage variation in the rest of the circuit, square waves can be assumed on the capacitors. Therefore, a square wave source just after the piezoelectric transformer (T_{pzt} is assumed constant similarly to the transformer ratio in Figure 7) is used. Here, T_{pzt} is constant over frequencies ranging from 0 to frequencies higher than the first mode, i.e. more than 10 times higher than the first harmonic of our square wave. This means that for the first 10 harmonics of the square wave T_{pzt} is constant, and distortion will only affect harmonics after the 10th one. Such a distortion will not modify the square wave since most energy is distributed over the first 10 harmonics.

Next, Thevenin's theorem is applied to the circuit in Figure 8a, and an equivalent circuit is obtained in Figure 8b by neglecting PZT damping and equivalent mass.

Applying a square wave to this RLC circuit, θ and $\dot{\theta}$ behavior is observed as given in Figure 9. Although we are in the linear case, waveforms are distorted sinusoids. In the linear case, the output can be thought as a square wave filtered by the second order system. The filter is a resonant one, and L_{wing} and $N^2 C_{stiff}$ are designed to resonate at 150 Hz . The output's most relevant harmonic is the first (a sine at 150Hz, tuned with the resonant frequency of the filter) while the others will be attenuated. Therefore, higher harmonics are present with a small amount of energy, and their contribution leads to a distorted sine. By choosing a square wave with a different duty cycle, it is possible to have an input with different energy distributions among harmonics so that θ can be reshaped.
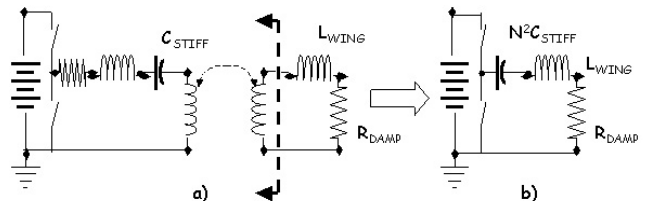

Figure 8: (a) Thevenin's theorem for linear networks is applied to the part of network on the left of the dashed line and so it is independent on the load whether it is linear or not. b) After applying Thevenin's theorem, only the capacitor is left since PZT damping and equivalent mass (resistor and inductor) are negligible compared to the load damping and inertia.
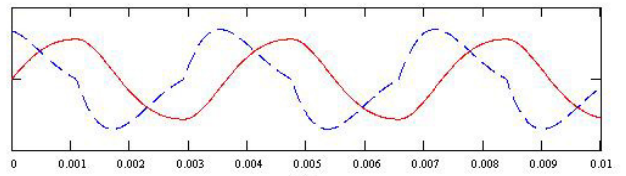

Figure 9: Simulated wing stroke angle ϕ (solid line) and angular speed $\dot{\phi}$ (dashed line) shapes using a square wave drive.

Piezoelectric actuators exhibit parasitic capacitance and many problematic power issues arise from charging or discharging such a capacitor by means of a constant voltage source and a switching stage. In [16], Athas *et al* showed that capacitors can be charged efficiently with a voltage ramp (*i.e.* a constant current source) but circuits for generating such an input tend to dissipate too much energy in the power supply itself, even without a load. The basic operation of a simple charge recovery system is shown in Figure 10. This circuit introduces an inductor into the system to take advantage of the oscillatory nature of LC circuits. When the switch is closed, the voltage across the capacitor is reversed. A proof-of-concept experiment using low voltage and a real capacitor, rather than a piezo, is shown in Figure 10d.

5 Actuator Characterization

During the experiments, unipolar input voltages are applied to diminish hysteresis and depolarization problems.
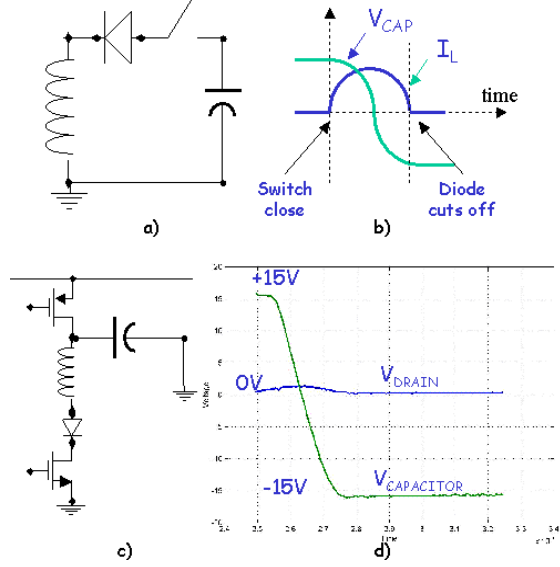
Figure 10: (a) LC oscillating circuit when current is positive; (b) inductor current and capacitor voltage vs. time; (c) implemented circuit; and (d) acquired waveforms from circuit.

The unimorph tip deflection is measured using an optical detection system as shown in Figure 11. In this setup, a horizontal helium neon laser beam is focused onto a perpendicular 1-D photo diode array (SL5-2, UDT Sensors Inc.). Then, the unimorph tip is positioned in between so that the tip motion is measured by the motion of its shadow on the sensor. A dynamic signal analyzer (HP-3562A) is utilized for frequency response characteristic measurements. For quasi-static measurements a PC-based real-time $(10 - 15\ KHz)$ ADC and DAC board (MultiQ data acquisition board, Quanser Consulting Inc.) is used in a Simulink programming environment.

The blocking force is measured with a semiconductor strain gauge (Entran Inc., ESB-020) glued on the base of a rigid brass beam where the setup is shown in Figure 12. The unimorph tip is contacted to the beam end, and the perpendicular force at the beam is measured as F_1. The actuator output force also bends the flexible brass beam with δ_1 displacement, and this bending is measured by a side view optical microscope. Thus, measuring the free deflection δ_{dc} previously, F_b is computed from

$$F_b = \frac{F_1}{1 - \delta_1/\delta_{dc}} \tag{13}$$

For prototype $16 \times 3 \times 0.21\ mm^3$ PZT-5H and $5 \times 1 \times 0.22\ mm^3$ PZN-PT unimorphs, all parameters are measured, and compared with the theoretical results as given in Table 3. Here, superscript t denotes the theoretical values, and f_r is measured at $V = 12\ V$. For each unimorph, $h_s = 76\ \mu m$. The experimental resonant frequency and blocking forces are lower than the theoretical ones, due to the nonlinearities at high voltages. On the other hand, although δ_{dc} of the PZN-PT unimorph is around 4 times less than the PZT-5H one, it rotates
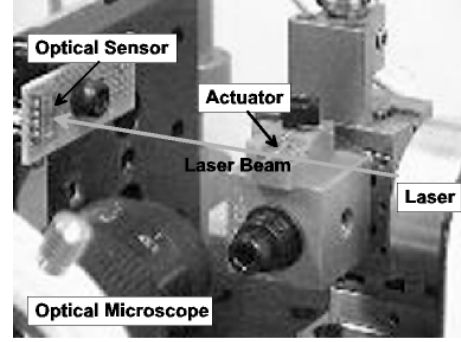

Figure 11: Optical detection setup with the laser and photodiode detector for actuator deflection measurements.
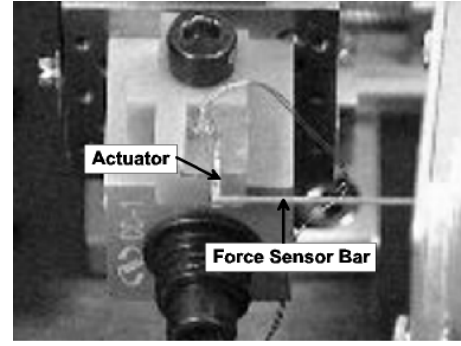

Figure 12: The photo of the blocking force measurement setup with a rigid brass beam and a strain gauge on it.

1.25 times more since it is 3 times shorter. Thus, if the proper T is selected as shown in Table 2, PZN-PT and PZT unimorphs could have a similar flapping actuation performance while the PZN-PT unimorph is around 8 times less in size and weight.

The electrical hysteresis of a $10 \times 1 \times 0.15\ mm^3$ size PZT-5H unimorph is measured using the circuit with a series resistor and sinusoidal input as illustrated in Figure 13a. Here, the charge in the piezo actuator is integrated from the measured current. Resulting charge hysteresis is displayed in Figure 13b. The hysteretic area corresponds to the dissipated energy by the hysteretic capacitor during a charging and discharging cycle, and it is computed as $0.6\ mW$ at $150\ Hz$. This value is small compared to the theoretical $10\ mW$ total output power on the load.

The effect of increasing the electric field on the mechanical hysteresis measured at $1\ Hz$ is shown in Figure 14. As can be seen in the figure, mechanical hysteresis, i.e. the structural damping, increases by the higher voltage.

For the dynamic response characteristic, the frequency response plots (amplitude and phase) are illustrated in Figure 15, and from the plot, f_r and Q can be computed. As can be seen from the figures, f_r and Q are lowered by increasing the input voltage. This effect could be due to

	V	δ_{dc}	δ_{dc}^t	F_b	F_b^t	f_r	f_r^t	Q
	(V)	(μm)	(μm)	(mN)	(mN)	(Hz)	(Hz)	
PZT-5H	150	408	354	51	55	395	463	21
PZN-PT	200	96	118	41	77	2004	2897	41

Table 3. Measured and theoretical values for prototype PZT-5H and PZN-PT unimorphs.

(a)

(b)
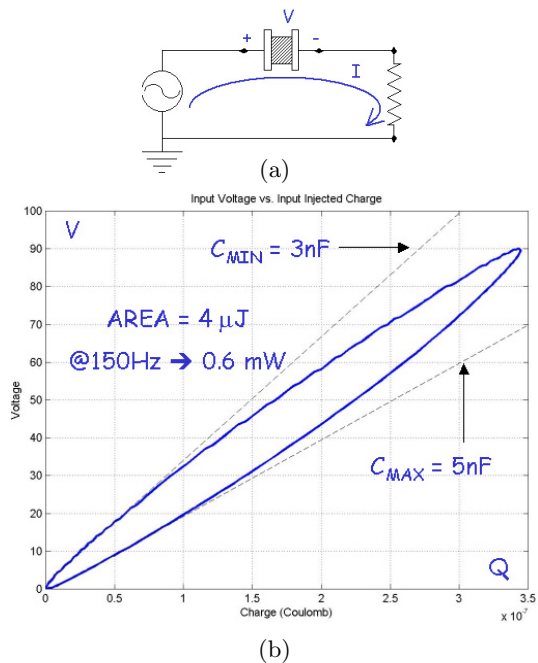
Figure 13: Measured electrical hysteresis behavior of a $10 \times 1 \times 0.15$ mm^3 size PZT-5H unimorph.

the nonlinear behavior of the actuator where the piezoelectric layer stiffness is decreased by the increased field [12]. This stiffness change is also observed for our unimorphs as displayed in Figure 16. The PZN-PT becomes relatively more compliant at the increased electric field with respect to the PZT-5H unimorph.

6 Conclusion

Development of the unimorph actuators for a microaerial flapping mechanism is discussed. PZT-5H and PZN-PT are investigated as the piezoelectric layers of the unimorph actuator. Design issues for microaerial flapping actuators, and actuator dimensions are determined for biomimetic wing actuation. $16 \times 3 \times 0.21$ mm^3 PZT and $5 \times 1 \times 0.22$ mm^3 PZN-PT unimorphs are fabricated,
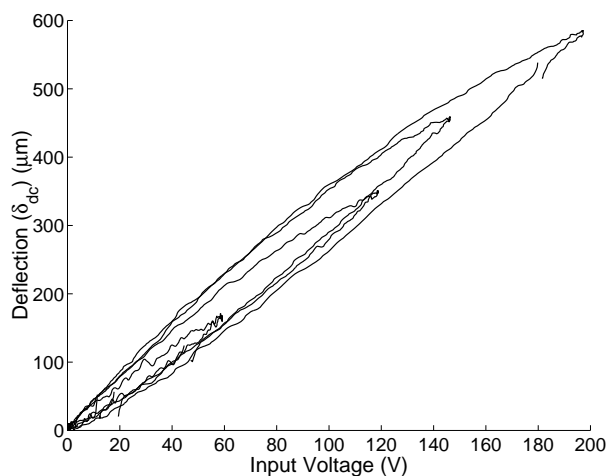

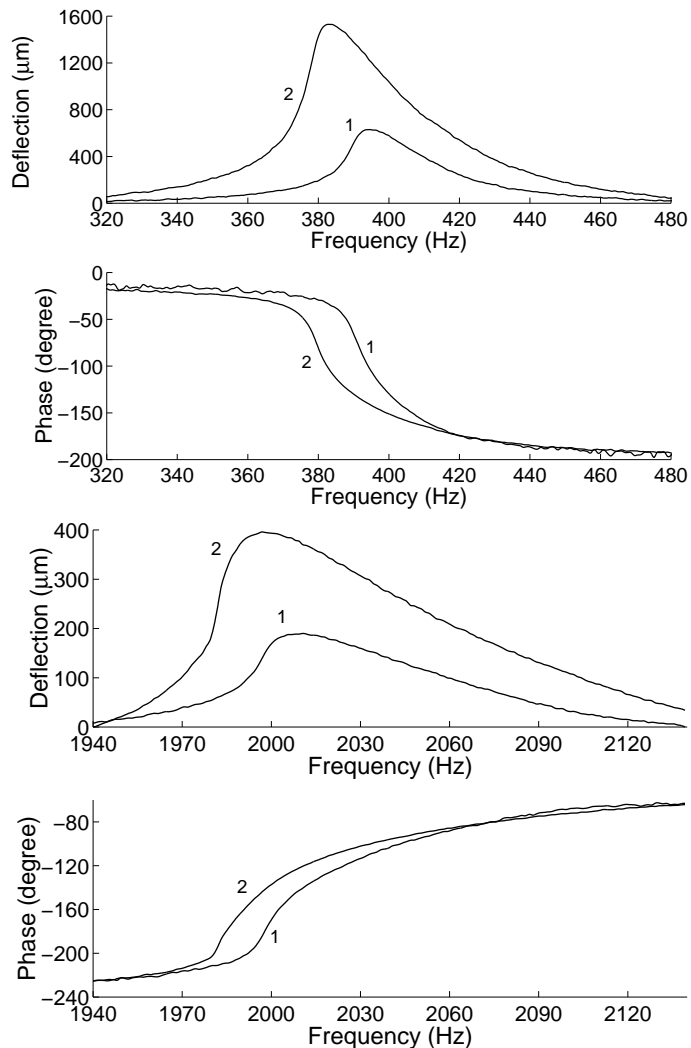Figure 14: Mechanical hysteresis curves of the PZT-5H unimorph at quasi-static mode (1 Hz) for different voltages.

Figure 15: Shift in the resonant frequencies of the PZT (upper) and PZN-PT (lower) unimorphs depending on the applied voltage (1: $V = 12$ V, 2: $V = 30$ V).

and their performances are tested. Nonlinear behavior of the piezos are observed at high electric fields. A 1 d.o.f. wing flapping mechanism is actuated by the PZT-5H unimorph with $V = 85$ V, and $180°$ stroke angle is achieved at 95 Hz which shows the success of the unimorph design (Figure 17).

In order to increase the displacement and output torque performance of the unimorphs with smaller dimensions, prestressing could be a possible solution which is future work. Moreover, switching-based low-loss driving electronics for the actuators will be fabricated as an on-board module using microelectronics technologies. Then, a compact and light weight microaerial robot actuation mechanism would become possible.
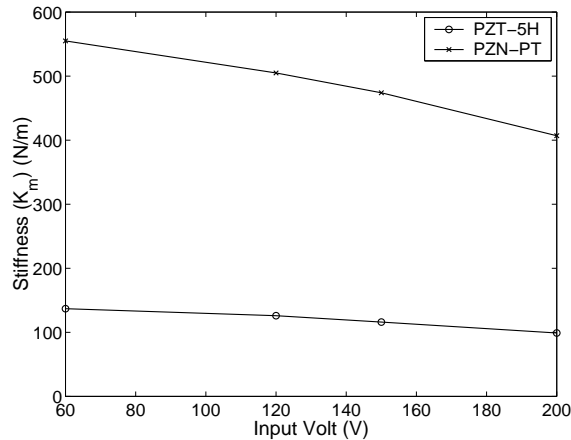
Figure 16: The nonlinear drop in the mechanical stiffnesses of PZT-5H and PZN-PT unimorphs by the increasing input voltage.

References

[1] R. Fearing, K. Chiang, M. Dickinson, D. Pick, M. Sitti, and J. Yan, "Transmission mechanism for a micromechanical flying insect," in *Proc. of the IEEE Int. Conf. on Robotics and Automation*, San Francisco, USA, Apr. 2000.

[2] E. Precht and S. Hall, "Design of a high efficiency, large stroke, electromechanical actuator," *Smart Mater. Struct.*, vol. 8, pp. 13–30, 1999.

[3] J. Yan, R. Wood, S. Avadhanula, M. Sitti, and R. Fearing, "Towards flapping wing control for a micromechanical flying insect," in *Proc. of the IEEE Int. Conf. on Robotics and Automation*, Korea, 2001 (to appear).

[4] M. Goldfarb and N. Celanovic, "Modelling piezoelectric stack actuator for control of micromanipulation," *IEEE Control System Magazine*, vol. 17, no. 3, pp. 69–79, 1997.

[5] Q. Wang, X. Du, B. Xu, and L. Cross, "Theoretical analysis of the sensor effect of cantilever piezoelectric benders," *J. of Aplied Physics*, vol. 85, pp. 1702–1712, 1 Feb. 1999.

[6] M. Sitti, "PZT actuated four-bar mechanism with two flexible links for micromechanical flying insect thorax," in *Proc. of the IEEE Int. Conf. on Robotics and Automation*, Korea, 2001 (to appear).

[7] A. Cox, D. Monopoli, and M. Goldfarb, "Development of piezoelectrically actuated elastodynamic flapping microaerial devices," in *ASME Adaptive Structures and Material Systems*, pp. 257–262, 1999.

[8] J. Smits and W. Choi, "The constituent equations of piezoelectric heterogenous bimorphs," *IEEE Tran. on Ultrasonics, Ferroelectrics, and Freq. Control*, vol. 38, pp. 256–270, May 1991.

[9] M. Weinberg, "Working equations for piezoelectric actuators and sensors," *Journal of Microelectromechanical Systems*, vol. 8, pp. 529–533, Dec. 1999.
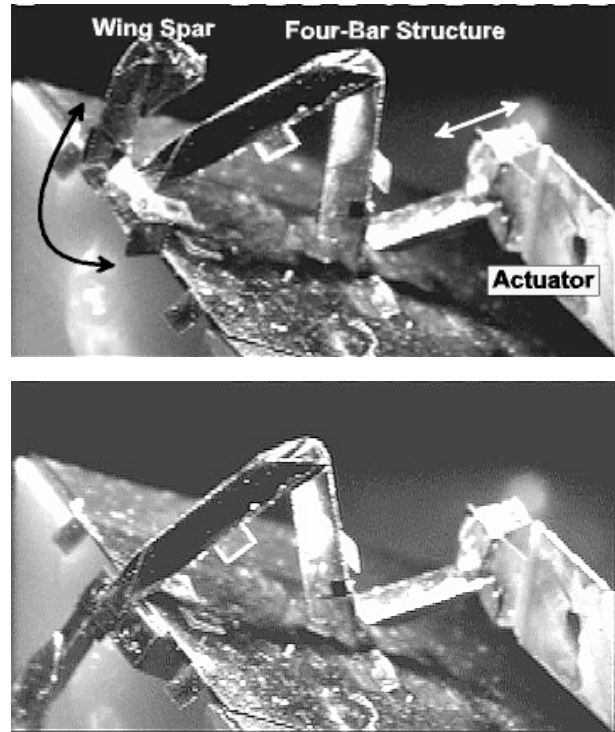

Figure 17: A 1 d.o.f. flapping wing experimental result using the PZT-5H unimorph actuators: up (upper image) and down (lower image) strokes of the wing spar where $180°$ stroke angle is achieved at $95\ Hz$.

[10] J. Smits and A. Ballato, "Dynamic admittance matrix of piezoelectric cantilever bimorphs," *Journal of Microelectromechanical Systems*, vol. 3, pp. 105–111, Sept. 1994.

[11] J. Smits, W. Choi, and A. Ballato, "Resonance and antiresonance of symmetric and asymmetric cantilevered piezoelectric flexors," *IEEE Trans. on Ultrasonics, Ferr. and Freq. Control*, vol. 44, pp. 250–258, March 1997.

[12] Q. Wang, Q. Zhang, B. Xu, R. Liu, and L. Cross, "Nonlinear piezoelectric behavior of ceramic bending mode actuators under strong electric fields," *Journal of Applied Physics*, vol. 86, pp. 3352–3360, 15 Sept. 1999.

[13] Q. Wang, X. Du, B. Xu, and L. Cross, "Electromechanical coupling and output efficiency of piezoelectric bending actuators," *IEEE Trans. on Ultrasonics, Ferro. and Freq. Control*, vol. 46, pp. 638–646, May 1999.

[14] S. Liu, S. Park, T. Shrout, and L. Cross, "Electric field dependence of piezoelectric properties for rhombohedral $0.955Pb(Zn_{1/3}/Nb_{2/3}/)O_3/-0.045PbTiO_3/$ single crystals," *Journal of Applied Physics*, vol. 85, no. 5, pp. 2810–14, 1999.

[15] O. Sotavalta, "The wing stroke frequency of insects in wing mutilation and loading experiments at subatmospheric pressure," *Ann. Zool. Soc.*, vol. 15, no. 2, pp. 1–67, 1952.

[16] W. Athas, J.G.Koller, and L. Svensson, "An energy efficient CMOS line driver using adiabatic switching," in *Proc. of the Fourth Great Lakes Symp. on VLSI. Design Automation of High Performance VLSI Systems GLSV*, p. 1994.